Short Communication

Process development for the hybrid additive manufacturing of metallic structures on polymer substrates

Steffen Czink [a],[*], Victor Lubkowitz [b], Stefan Dietrich [a], Volker Schulze [a]

[a] *Institute for Applied Materials (IAM-WK), Engelbert-Arnold-Straße 4, Karlsruhe 76131, Germany*
[b] *wbk Institute of Production Science, Kaiserstrasse 12, Karlsruhe 76131, Germany*

ARTICLE INFO	ABSTRACT
	3D hybrid additive manufacturing describes the combined application of different additive manufacturing processes in order to manufacture a component with almost unlimited design freedom and free choice of materials. One challenge in the hybrid additive manufacturing lies in the different conditions of individual additive manufacturing processes. For example, in the combined application of the laser powder bed fusion (PBF-LB) of metals with the fused filament fabrication (FFF) of polymers, damage can occur in the plastic due to the higher processing temperatures of PBF-LB. Therefore, in this work a process strategy for the buildup of metallic structures in the PBF-LB process on polymer base structures was developed. By reducing the laser energy density in combination with increasing the height of the first layer, a processing window could be identified. The built hybrid components were investigated with micro-computed tomography and the effects of different processing parameters on the interface between the polymer and metal part are discussed. Finally, a strategy to increase the strength of the interface is presented.

1. Introduction

With additive manufacturing technologies (AM), it is possible to increase the design flexibility of components compared to conventional subtractive machining. Therefore, AM has progressed from a rapid prototyping process to an industrial manufacturing technique [1]. In AM technologies, the component usually is made from one material by applying it layer by layer. Polymers are mainly manufactured additively in the Fused Filament Fabrication (FFF) process. In this process, a plastic filament (for example PLA or ABS) is melted and applied layerwise to a platform using an extruder nozzle. A common additive manufacturing process for metallic components is Laser Powder Bed Fusion (PBF-LB). In this process, fine powder is applied layer by layer to a base plate by a recoater and then fused locally by a high energy laser beam [2]. Frequently used alloys in the PBF-LB process are AlSi10Mg, stainless steel 316l, IN718 or Ti6Al4V.

The combination of different AM processes for different materials is called hybrid additive manufacturing and enables an increase in design freedom such as function integration as well as the possibility of specifically tailoring the component's properties (e.g. varying density or thermal and mechanical properties). The hybridization of purely metallic structures is already been widely researched and has already reached a Technology Readiness Level (TRL) of 4 to 5 [3]. For example Girnth et al. developed a hybrid-material powder coating system to combine the

manufacturing of two metals in the PBF-LB process [4]. The manufacturing of a zirconia-alumina ceramic on an as-built surface of tool steel in the PBF-LB process was investigated by [5]. Feldhausen et al. developed a strategy of embedding ceramics in 316L stainless steel manufactured in the Direct Energy Deposition (DED) process [6]. The study revealed that the introduction of unmelted powder provides a thermal barrier to protect the ceramic substrate in the DED process [6]. The deposition of the subsequent metal layer with an oblique angle for the print head further diverts the thermal energy to the powder instead of directly to the ceramic insert [6]. Examples of successful implementation of hybridization within the polymer material class is known as multi-material FFF, in which different thermoplastics are processed, or the combination of the Digital Light Processing (DLP) with an InkJet printing system to manufacture electronic components [7,8].

With the hybrid manufacturing of polymers and metals, the functionality and flexibility of components can be increased further [9]. By applying the single material classes at individual component areas, customized functions such as damping or electrical insulation can be integrated. However, due to the different processing conditions of the material classes, a hybridization of polymers and metals can be challenging. Currently, hybridization of simple geometries of metals and polymers is performed extrinsically by joining techniques. In addition, Baranowski et al. have shown the possibility of intrinsic hybridization of more complex geometries by integrating metallic or electronic subcomponents in

---

the FFF process [10]. Kurfess et al. developed a strategy of increasing the design flexibility of the DED process by manufacturing 316L stainless steel onto polymer-based substrates [11]. For the reduction of the polymer degradation, a cooling time between the deposition of each layer was introduced [11]. For the combination of the PBF-LB with the FFF process, only a few works exist. In the work of Chueh et al., a multi material 3D printing system is presented, which is able to combine the FFF process with the PBF-LB process in one machine [12]. To connect PBF-LB with the FFF areas, structures in the size of several millimeters were built up in the PBF-LB process, which then created an interlocking connection with the polymer from the FFF process. The work of Englert et al. for the first time investigated metallic structures in the submillimeter scale onto which the polymer part was applied in the FFF process [13]. The approach led to a tensile strength of the interface between FFF PLA and PBF-LB AlSi10Mg of more than 20 MPa [13]. However, to build metallic PBF-LB structures on a polymer substrate is still challenging. The processing temperatures of the PBF-LB process of metals is much higher than the degradation temperature of most polymers. Only if this sequence of additive buildup is also successful, a complete 3D hybridization of metals and polymers in additive manufacturing is possible. The work of Chueh et al. showed that by adding steel particles to the polymer filament, it is possible to build copper (Cu10Sn) structures on the polymer part [12]. However, the addition of metal particles restricts the design flexibility of the hybrid additive manufacturing by, for example, eliminating the electrically insulating effect of the plastic.

The aim of this study is to fabricate metallic AlSi10Mg structures on ABS plastic substrates without adding metal particles. The aluminum material was chosen due to its lower melting temperature of around 595 ˚C compared to steel materials, which are also used in the PBF-LB process [14]. The ABS plastic was chosen because of its relatively high degradation temperature of around 400 ˚C and its good processability in the FFF process compared to high temperature plastics such as PEEK [15]. This combination of materials minimizes the thermal mismatch, but does not eliminate it. Numerical simulations reveal that in the PBF-LB process even much higher temperatures than the melting temperature of AlSi10Mg occur, which may reach up to 1800 ˚C [16,17].

In this study, in a first stage a strategy was developed for creating an initial bond between the AlSi10Mg structures and the ABS substrate. To reduce the thermal degradation of the ABS, the thickness of the first PBF-LB layer was increased and the PBF-LB processing parameters were changed to reduce the total energy input into the samples. To analyze the interface between polymer and metal, micro-computed tomography (µCT) investigations of built samples under different processing parameters were carried out. In a second stage, a strategy including the FFF process was developed to increase the stability of the initial bond between ABS and AlSi10Mg, thus making the manufacturing of a complete hybrid component possible.

2. Materials and methods

2.1. Materials

For manufacturing the PBF-LB parts of the samples discussed in this work, AlSi10Mg powder supplied from m4p material solutions GmbH (Magdeburg, Germany) with a powder bulk density of $1.51 \, \text{gm cm}^{-3}$ was used. Table 1 shows the chemical composition of the powder. The size distribution of the particles is given in Fig. 1 and shows $D_{10} = 20.0 \, \mu\text{m}$, $D_{50} = 37.4 \, \mu\text{m}$ and $D_{90} = 54.4 \, \mu\text{m}$.
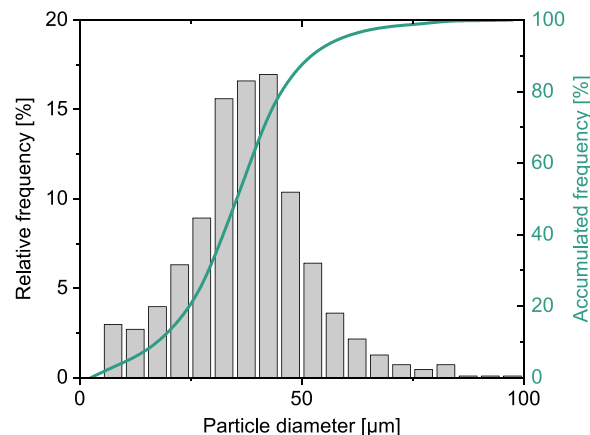
Fig. 1. Particle size distribution of the AlSi10Mg powder used for manufacturing the PBF-LB parts of the samples shown in this work.

ABS plates with a thickness of 5 mm supplied by S-Polytech GmbH (Kranenburg, Germany) were used as substrate for the buildup of the initial AlSi10Mg structures. The plates were machined to a round shape with a diameter of 110 mm and then mounted to a conventional PBF-LB aluminum base plate.

The FFF processing was performed using Ultrafuse ABS filament from BASF (Ludwigshafen, Germnay) [18]. The filament has a recommended nozzle temperature of 240–260 ˚C and a bed temperature of 90–110 ˚C. The recommended print speed is $40–80 \, \text{mm s}^{-1}$.

2.2. Sample processing

The PBF-LB processing in this study was done with a Creator developed by O.R. Lasertechnologie GmbH (now 2oneLab GmbH, Darmstadt, Germany). The PBF-LB machine is equipped with an Ytterbium fiber laser (YLM-150) with a maximum power of 250 W and a wavelength of 1070 nm. The machine supports round base plates with a diameter of 110 mm which cannot be heated. An F-theta lens ensures a constant spot diameter across the base plate. After each layer, fresh powder is spread over the base plate with a rotary recoater which can be aligned with micrometer screws. To prevent oxidation, the building process is carried out in Argon atmosphere with an oxygen content < 0.1%.

A custom made FFF machine "Flexibel3D" was used for the FFF printing in this study. The FFF machine has a direct drive extruder with an E3D-v6 hotend and a nozzle diameter of 0.4 mm, which can be heated to a temperature of maximum 280 ˚C. The maximum movement speed of the extruder is $100 \, \text{mm s}^{-1}$. The machine works with a Duet 2 Ethernet electronic board with the firmware RepRap 2.05. The base plate has a size of $215 \times 215 \, \text{mm}^2$ and can be heated up to 120 ˚C. Parts with a maximum height of 210 mm can be manufactured. The PrusaSlicer in the version 2.4.2 was used for creating the GCODE of the FFF part.

2.3. Thermogravimetric analysis

The thermal degradation behavior of the ABS base plates used in this work was studied with a thermogravimetric analysis (TGA). Therefore, a sample in the size of around $5 \times 5 \times 5 \, \text{mm}^3$ was machined out of an ABS base plate. The TGA was performed in a STA 449 F1 Jupiter

Table 1
Chemical composition of the AlSi10Mg powder particles in wt.%.

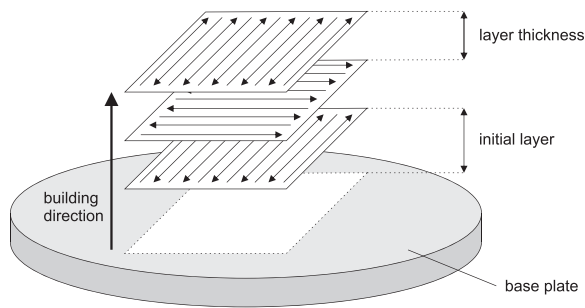| Al	Fe	Si	Mg	Mn	Ti	Zi	Cu	Pb	Sn	Ni
Base	0.16	9.3	0.25	< 0.01	< 0.01	< 0.01	< 0.01	< 0.01	< 0.01	< 0.01

Fig. 2. Scanning strategy for the parameter optimization in the hybrid additive manufacturing.

from NETZSCH-Gerätebau GmbH (Selb, Germany) with a heating rate of $1 \, \mathrm{K \, min^{-1}}$ under Argon atmosphere with a purge of $50 \, \mathrm{mL \, min^{-1}}$.

2.4. Micro-computed tomography

μCT images were recorded for a detailed investigation of the material interfaces from the hybrid additive manufacturing process. The μCT system PRECISION developed by YXLON International GmbH (Hamburg, Germany) was used for the investigation. A target current of 0.06 mA combined with an acceleration Voltage of 165 kV were used to generate the x-ray beam for scanning the samples, leading to a tube power of about 10 W. A flat panel detector Perkin Elmer XRD1620 AN with a pixel pitch of 200 μm and a total size of 2048x2048 pixels was used to capture the intensity of the x-rays. A focus object distance (FOD) of 62.2 mm and a focus detector distance (FDD) of 1331.7 mm were used, leading to a voxel size of 9.3 μm. 1860 projections were captured in each scan. For each projection, binning of two frames with an integration time of 750 ms was applied to reduce noise. 3D images were reconstructed using a filtered back projection (FBP) algorithm in VGStudioMAX 3.4 by Volume Graphics international GmbH (Heidelberg, Germany). For further noise reduction, a median filter was applied to the reconstructed 3D images. A region growing algorithm, which is implemented in VGStudioMAX was used to segment gaseous phases such as ambient air and voids from AlSi10Mg and ABS. The degradation of the ABS due to the thermal load of the PBF-LB process (see Section 1) results in the formation of porosity in the ABS base plate. The porosity was analyzed with the VGEasyPore module implemented in VGStudioMAX. During the analysis, pores with a volume smaller than 8 voxel (2x2x2) were discarded to further reduce noise.

3. Process development

In this work, a strategy consisting of two stages for manufacturing PBF-LB structures on an ABS base plate was developed. The goal of the first stage was to create an initial bond of the built AlSi10Mg structures. Therefore, samples with the dimension of $6 \times 6 \times 6 \, \mathrm{mm^3}$ were manufactured with different processing parameters in the PBF-LB process. A bidirectional line scanning strategy without perimeter scan was used for manufacturing the samples. Between two subsequent layers, the scan vectors were alternating between a 0° and a 90° orientation to ensure a homogeneous distribution of the thermal load across each layer (see Fig. 2). This strategy avoids overheating in the corners of individual layers due to a concentration of short scan vectors compared to the standard scanning strategy with a 67° pattern rotation as used in most PBF-LB systems. To protect the ABS from the high thermal load of the PBF-LB process, the initial layer was scanned with an increased thickness, which was varied from 300–500 μm. To ensure a constant thickness of the initial layer across the base plate, the recoater of the PBF-LB machine was aligned individually for each base plate used. For the subsequent layers in the building process, a thickness from 100–150 μm was used. Additionally, the laser power was varied from 135–210 W, the hatch spacing

from 150–400 μm. For all samples, the scanning speed of $600 \, \mathrm{mm \, s^{-1}}$ and the nominal spot diameter of 40 μm were kept constant.

To increase the strength of the interface between the ABS and AlSi10Mg, the initially built AlSi10Mg structures were stabilized in a second stage of this study using the FFF process. With this sequential procedure a mechanical form-fit between the polymer and the metal part can be achieved. The procedure is schematically shown in Figure 3. Therefore, rectangular structures in the size of $6 \times 6 \times 2 \, \mathrm{mm^3}$ were built on an ABS base plate in the PBF-LB process using optimized parameters from the initial parameter study. The PBF-LB process then was interrupted and a stabilizing structure of the same height was built around the initial AlSi10Mg parts in the FFF process. The different coordinate systems of the two machines used in the hybrid process represent a major challenge. Therefore, a ring of ABS was first printed onto the bed of the FFF machine, into which the ABS plate used for the hybrid process was inserted. A base plate temperature of 100 °C was used to fabricate the FFF parts of the component. After inserting the ABS plate in the positioning ring, a soaking time of 15 min was identified to ensure a constant temperature distribution across the base plate. FFF printing was performed with a nozzle temperature of 240 °C and a movement speed of $50 \, \mathrm{mm \, s^{-1}}$. To prevent the nozzle from colliding with the initially built AlSi10Mg part, the nozzle was raised by 3 mm along the building direction for movements outside the contour of the FFF area. In the next step, the upper surface of the initial AlSi10Mg structure was overprinted with a single FFF layer (step (c) in Fig. 3). To further prevent a collision between the nozzle and the initial AlSi10Mg structure, additionally a layer thickness of 0.3 mm was selected for the FFF process. During the over printing step, the middle part of the initial AlSi10Mg structure was left free to serve as contact area for a continuation of the PBF-LB buildup (step (d) in Fig. 3). For this purpose, the entire base plate was transferred back to the PBF-LB machine, aligned and covered with powder until the top of the FFF part before the PBF-LB process was continued for another 4 mm.

4. Results and discussion

4.1. Thermogravimetric analysis

In Fig. 4, the TGA curve of the used ABS base plate material under Argon atmosphere is given. The degradation of the ABS takes place in a single step. The degradation temperature was defined as the range at which the mass loss is higher than 0.1 %/K. The degradation starts at around 340 °C and ends at around 450 °C. The residues at 450 °C and 1000 °C are 8.2% and 5.8%, respectively.

The degradation of the ABS plates used in this study starts about 255 °C below the melting temperature of AlSi10Mg of around 595 °C [14]. Numerical simulations reveal that in the PBF-LB process of AlSi10Mg even much higher temperatures - of up to 1800 °C - occur [16,17]. As a result of this high thermal load, massive degradation of the ABS substrate into gaseous products like styrene has to be expected in the PBF-LB process [19]. The formation of gaseous degradation products could lead to the removal of the AlSi10Mg powder particles and thus prevent the formation of solid structures. Therefore, an approach of increasing the thickness of the first layer in the PBF-LB process was chosen to protect the ABS from the thermal load.

4.2. Parameter optimization

In order to proof the creation of an initial bond of a PBF-LB AlSi10Mg structure on an ABS substrate, a systematic study of the PBF-LB processing parameters was carried out. The results of the study can be divided into three categories (see Fig. 5). In category I, only individual powder particles adhere to the surface of the ABS. Category II describes the successful buildup of initial AlSi10Mg structures on the ABS substrate. Category III depicts the ineffective buildup of AlSi10Mg structures. In
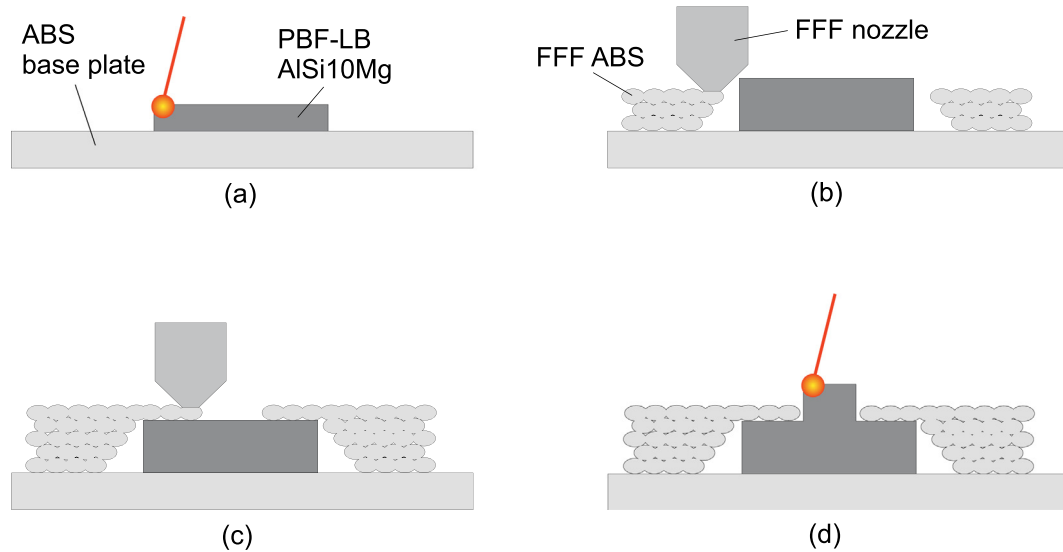
Fig. 3. Strategy development for the hybrid additive manufacturing of AlSi10Mg structures on ABS base plates. Building an initial AlSi10Mg structure (a). Interrupting the PBF-LB process and surrounding the initial AlSi10Mg structure in the FFF process (b). Overprinting the initial AlSi10Mg structure with a single FFF layer (c). Continuation of the PBF-LB process (d).
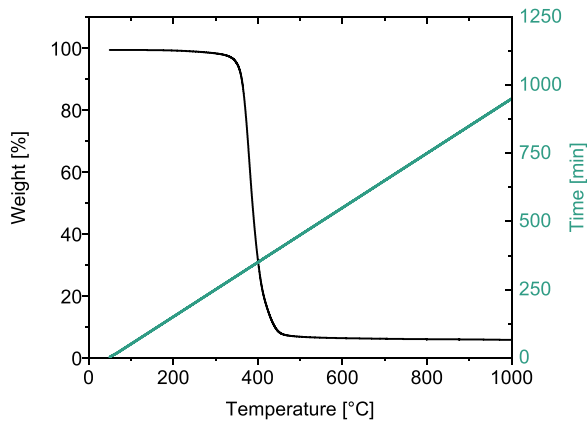

Fig. 4. TGA curve for the used ABS at a heating rate of $1\,\mathrm{K\,min^{-1}}$ under Argon atmosphere.

contrast to category I, a significantly stronger adhesion of powder particles to the surface of the ABS can be seen here. Additionally, a strong smoke development due to a massive degradation of the ABS was visible during the exposure. Similar results were also reported in the study of Chueh et al. building Cu10Sn structures on a PLA base plate [12].

In Fig. 6, the results of the parameter optimization for an initial layer of 500 μm are given. Only at individual parameter combinations initial AlSi10Mg structures could be built successfully (category II). The results can additionally be described with the laser energy density,

$$E_D = \frac{P}{vht} \tag{1}$$

where P is the laser power, v is the scanning speed, h is the hatch distance and t the layer thickness. Especially at low laser energy densities results of category I are observed due to the insufficient energy density for melting the powder particles. Raising the energy density by increasing the laser power and reducing the hatch distance, leads to a strong degradation of the ABS base plate and therefore to category III results. The results for an initial layer height of 300 μm are shown in Fig. 7. Similar to the results for an initial layer height of 500 μm, low laser energy densities mainly lead to category I results, whereas at high energy densities results of the category III are observed. However, for an initial layer height of 300 μm, a process window with successfully built AlSi10Mg structures (category II) can be identified. A layer thickness of 150 μm leads thereby to a wider process window compared to a layer thickness of 100 μm.

4.3. Micro-computed tomography

To investigate the interface between ABS and AlSi10Mg in detail, initial AlSi10Mg structures were examined using μCT. In Fig. 8(a), a reconstructed μCT image of an AlSi10Mg structure of category II is shown. The sample was built with an initial layer of 300 μm, a laser power of 165 W, a hatch distance of 250 μm and a layer thickness of 150 μm. These parameters represent the center of the identified processing window (see Fig. 7(b)) and were used to build all further samples discussed in this work. In the μCT image, the two components ABS and AlSi10Mg of the sample can be clearly identified by their different gray values. The AlSi10Mg part shows a high lack-of-fusion porosity of around 25% (see Fig. 8). The sample was built with a laser energy density of $7.3\,\mathrm{J\,mm^{-3}}$. For comparison, the typical laser energy density for AlSi10Mg in the PBF-LB process is around $60\,\mathrm{J\,mm^{-3}}$ [20], which would lead to a mas-
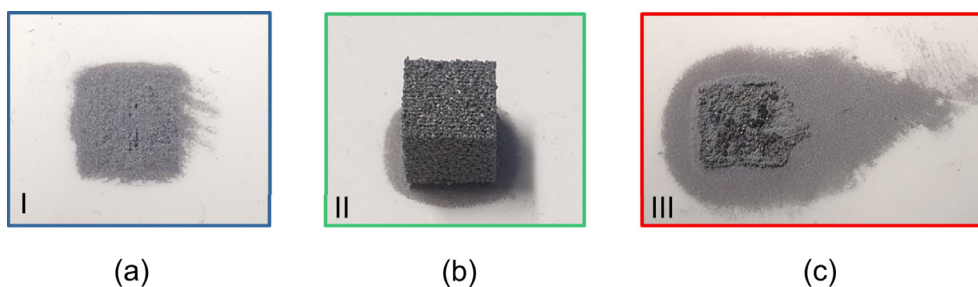

Fig. 5. Results of the parameter optimization for building AlSi10Mg structures on top of ABS substrate plates can be divided into three categories. Category I: Adhesion of loose powder particles to the ABS surface (a). Category II: AlSi10Mg samples built on top of ABS substrate (b). Category III: Significant damage to the ABS surface (c).
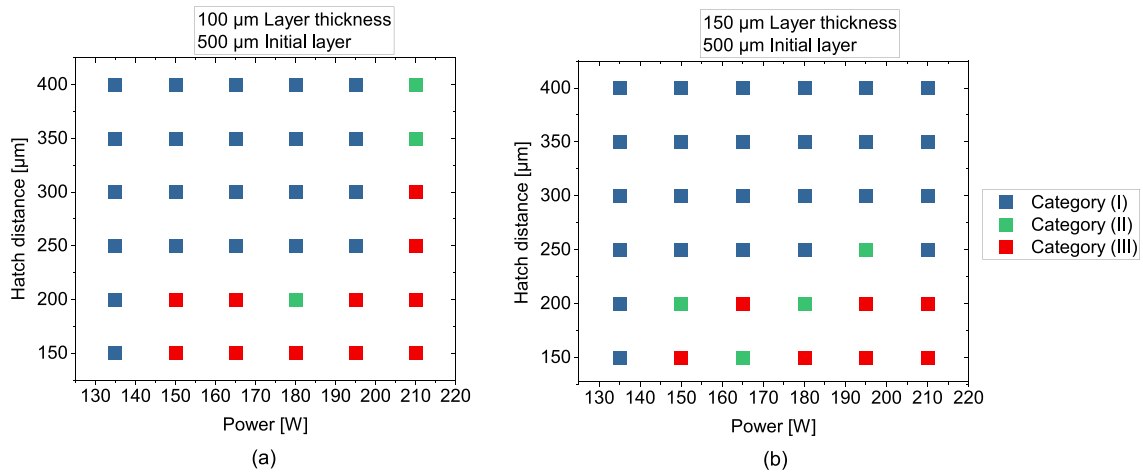
Fig. 6. Parameter optimization for an initial layer of 500 μm. Layer thickness of 100 μm (a). Layer thickness of 150 μm (b).
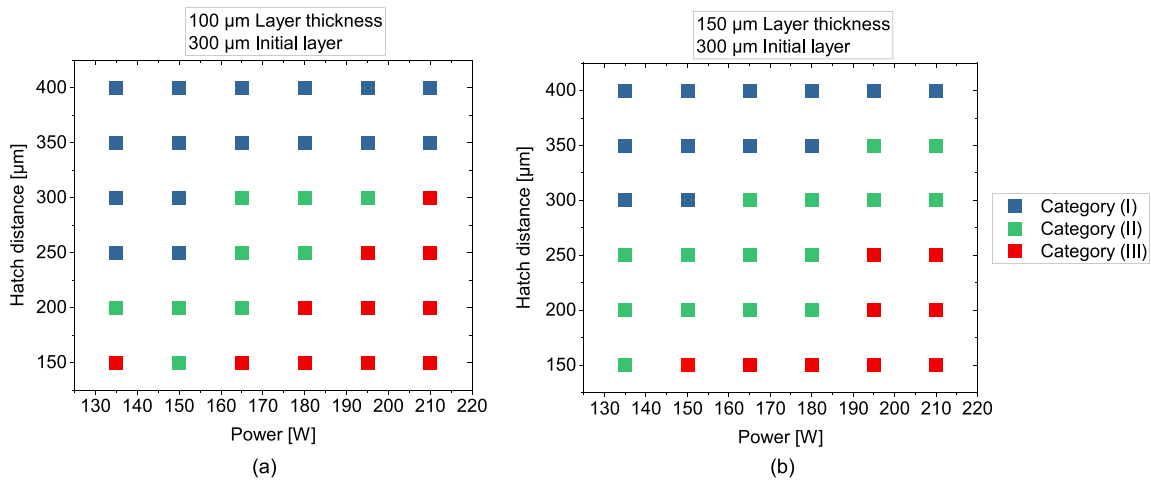

Fig. 7. Parameter optimization for an initial layer of 300 μm. Layer thickness of 100 μm (a). Layer thickness of 150 μm (b).
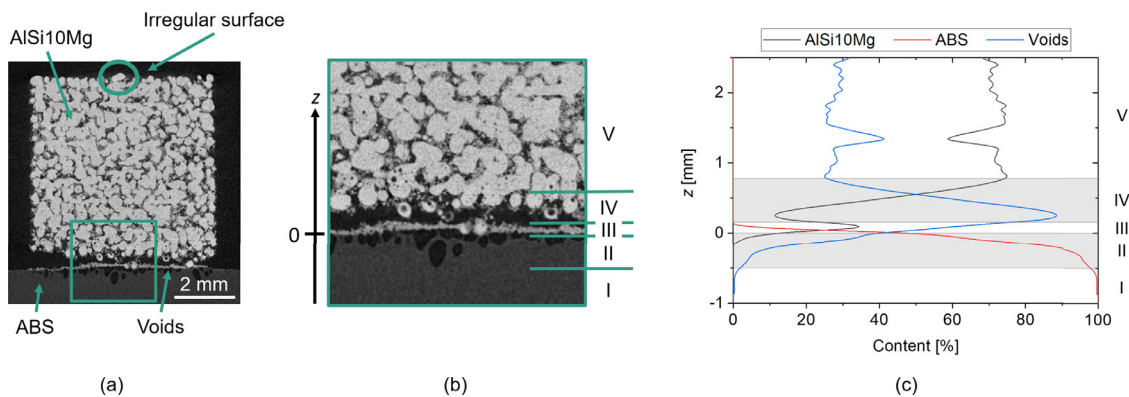

Fig. 8. Reconstructed μCT image of an AlSi10Mg structure on an ABS base plate (a). Interface between ABS and AlSi10Mg (b). Profile of the composition along the building direction z (c).

sive degradation of the ABS base plate in the hybrid process (see Fig. 7). Additionally, the top surface of the built AlSi10Mg structures show some irregularities, as illustrated in Fig. 8(a). In the coating process between two layers, these irregularities can lead to collisions with the recoater, which can cause the built AlSi10Mg structure to tear off from the ABS substrate. Therefore, increasing the layer thickness to 150 μm leads to a more stable buildup, as already shown in Fig. 7 [21].

In general, the interface between AlSi10Mg and ABS shows weak mechanical strength (see Fig. 8(b)). The AlSi10Mg part of the components can be detached from the ABS substrate manually using pliers. For a more detailed analysis of the interface, the individual components (AlSi10Mg, ABS and voids) were segmented using a region growing algorithm implemented in VGSTudioMAX. Figure 8(c) shows the profile of the composition along the building direction z. The upper surface of
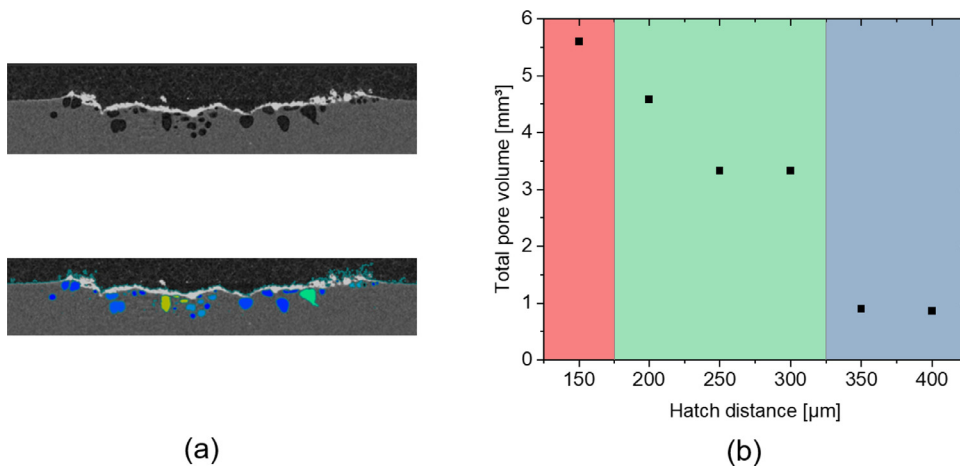
(a)

(b)

Fig. 9. Segmentation of the pores in the ABS (a) and total pore volume in the ABS of each sample as function of the hatch distance (b).
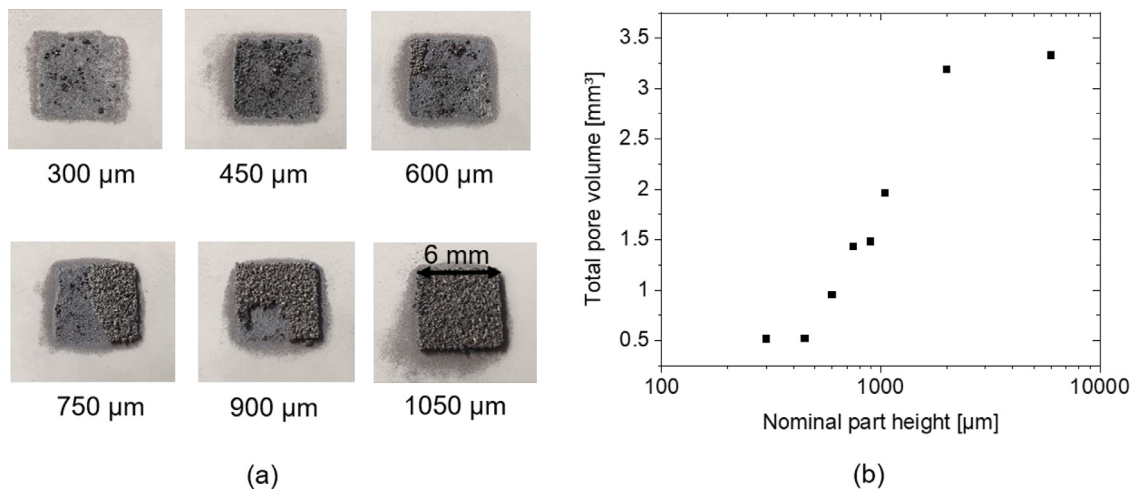

(a)

(b)

Fig. 10. Photographs of samples with a nominal height of 300–1050 μm (a) and total pore volume in the ABS part of each sample as a function of its nominal height (b).

the ABS substrate plate was defined as $z = 0$ mm. The profile can be divided into five zones along the building direction which are described in the following:

- **Zone I** describes the homogeneous ABS base plate.
- As a result of the high thermal load of the PBF-LB process, degradation occurs in the upper part of the ABS, which typically decomposes into gaseous products such as styrene [19]. This results in the formation of porosity which is described as **zone II**.
- Single AlSi10Mg powder particles are deposited on the surface of the ABS which is described by **zone III**. In some areas, the adhesion of consolidated AlSi10Mg can be identified.
- **Zone IV** describes the weak bond between consolidated AlSi10Mg particles connected to the ABS surface and the homogeneous AlSi10Mg structure.
- **Zone V** describes the homogeneous AlSi10Mg structure of the hybrid component.

As described earlier, the degradation of the ABS due to the thermal load of the PBF-LB process affects the buildup of solid AlSi10Mg parts on the ABS. To quantify the ABS degradation as a function of different parameters of the PBF-LB process, the total pore volume in the ABS of individual samples was determined from μCT images. In Fig. 9, the segmentation as well as the total pore volume in the ABS as function of the hatch distance are given. A clear decrease of the pore volume with increasing hatch distance can be observed. Additionally, the background was colored according to the results of the parameter optimization in

Fig. 5. Even for the results of category I, where the laser energy density is not sufficient for a consolidation of the metal powder, the formation of pores and therefore degradation of the ABS already takes place.

To investigate how the ABS degradation evolves during the PBF-LB process, AlSi10Mg samples with an area of 6×6 mm^2 and different nominal heights (300–6000 μm) were built onto ABS base plates and analyzed with μCT. In Fig. 10, a photograph of parts with a nominal height of 300–1050 μm (a), and the analyzed total pore volume of each sample as a function of the nominal height of each part (b) are shown. In the first three layers (300–600 μm), only powder and individual particles of consolidated AlSi10Mg are bonded to the ABS surface. It can be concluded that during the exposure of the fist layers the release of gaseous degradation products of the ABS impedes the buildup of a continuous AlSi10Mg structure. The buildup of a continuous AlSi10Mg structure starts during the exposure of the following layers (750–1050 μm), where the connection to the ABS is established by individual particles (see Fig. 8). The total pore volume in the ABS increases up to a nominal part height of 2000 μm. With further increasing part height, the pore volume in the ABS remains constant with around 3.3 mm^3. This indicates that no further degradation occurs in the ABS during the buildup process from a component height of 2 mm.

4.4. Stabilization of the ABS-AlSi10Mg interface

As can already be concluded from the μCT images presented in Section 4.3, the ABS-AlSi10Mg interface shows weak mechanical
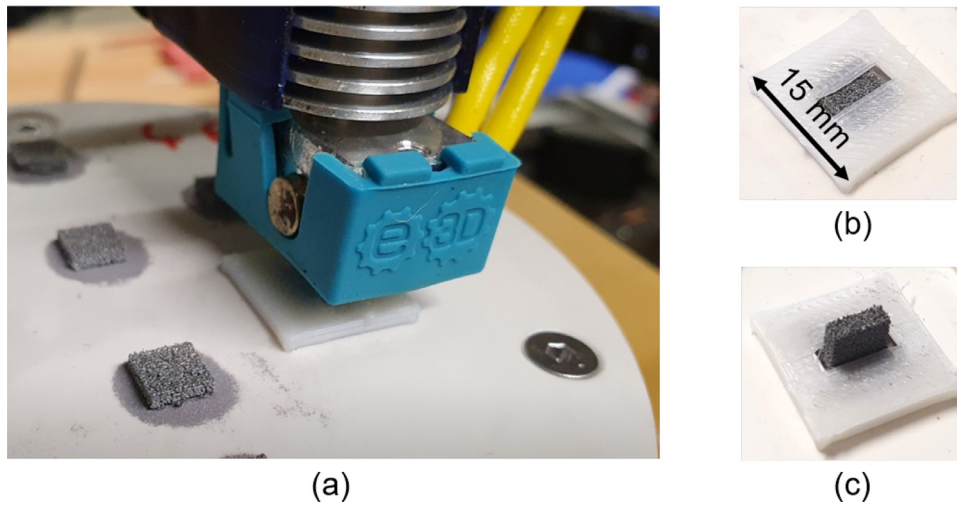
Fig. 11. Stabilization of the initially built AlSi10Mg structures in the FFF process (a). Photograph of a stabilized component (b) and hybrid component after continuation of the PBF-LB process (c).
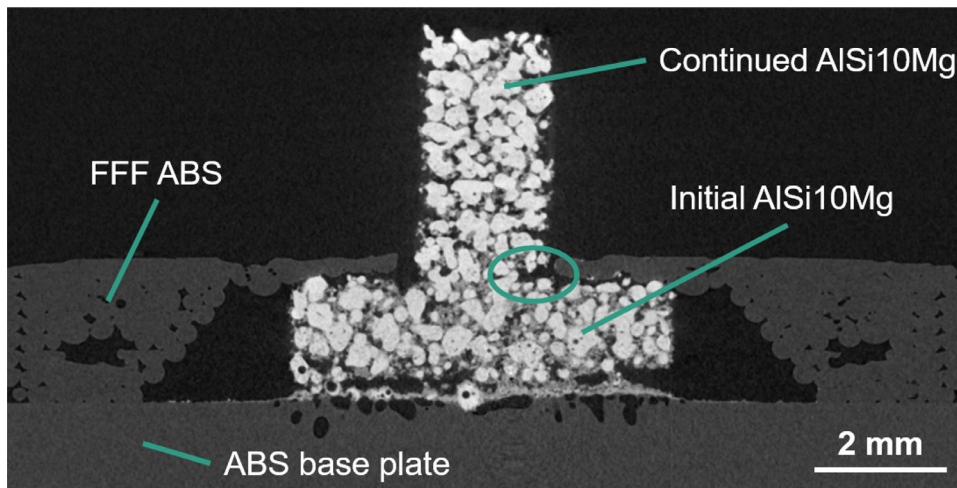

Fig. 12. Reconstructed µCT image of an ABS-AlSi10Mg hybrid structure.

stability. The initially built AlSi10Mg structures can be easily removed manually. Therefore, in a second stage, a form-fit was created using the FFF process as described in chapter 3. Although this strategy imposes some restrictions regarding the design freedom, it stabilizes the initially built AlSi10Mg structures. In the studies of Englert et al. and Leuteritz et al., which investigated the FFF buildup on top of metal parts, similar approaches already led to good mechanical properties of the hybrid interface [13,22]. For the PBF-LB process, the optimized parameters from the sample shown in Fig. 8 were used. In Fig. 11(a), a photograph of the stabilization process with a FFF machine of the initial AlSi10Mg part is shown. Figure 11(b) shows one component after printing the single ABS layer on top of the initial AlSi10Mg structure. After finishing the ABS layer, the parts were placed back into the building chamber of the PBF-LB system and covered with powder. During the overprinting of the initial built AlSi10Mg with a single FFF layer, the middle part of the AlSi10Mg surface was left free ($6 \times 2\,\mathrm{mm}^2$). This blank surface was then used as contact area for the continuation of the PBF-LB process for another 4 mm. A photograph of the finished hybrid structure is shown in Fig. 11(c). The finished hybrid structure was then machined out of the base plate analyzed using µCT.

Figure 12 shows an image of the reconstructed specimen. To capture the complete hybrid sample in the scan, the voxel size was set to 12.5 µm. The center clearly shows the initially built AlSi10Mg part including the five different zones as described in Fig. 8. To prevent a collision between the nozzle of the FFF machine and the initially built
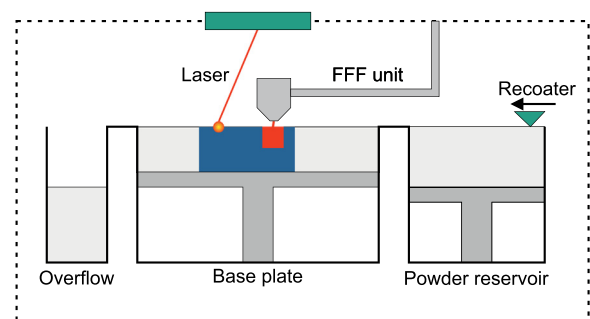

Fig. 13. Schematic drawing of the developed hybrid AM system combining the FFF and PBF-LB buildup.

AlSi10Mg structure, a gap had to be left between the initial AlSi0Mg structure and the surrounding FFF part. With a nozzle geometry adapted to the hybrid process and a reduced height of the initial AlSi10Mg part, the size of this gap could be reduced in future investigations. Additionally, the FFF ABS shows some fusion errors which might result from the adapted FFF strategy used in the stabilization process as described in chapter 3. Between the initially built and the continued AlSi10Mg structure, a bond could be established over wide areas. Nonetheless, isolated areas displaying a weaker bond persist, as depicted in Figure 12. A reduction in the thickness of the single FFF layer in the overprinting

step could improve the strength of the bond. Furthermore, by alternating multiple times between the PBF-LB and FFF process, as planned in a hybridized and automated machine setup, the stability of the hybrid structures could be improved.

5. Conclusion and outlook

In the first part of this study, different strategies for the buildup of initial AlSi10Mg structures in the PBF-LB process on ABS base plates as part of a novel hybrid PBF-LB and FFF manufacturing process were investigated. By scanning with a reduced volumetric laser energy density, compared to the conventional PBF-LB process, combined with increasing the thickness of the first layer, a stable process window for creating an initial bond of AlSi10Mg structures on ABS substrate could be identified. μCT analysis of the built AlSi10Mg structures revealed high lack of fusion porosity in the AlSi10Mg part. Porosity also occured in the ABS part due to degradation as a result of the high thermal load in the process. Furthermore, the interface shows a weak bond of the AlSi10Mg structure to the ABS base plate. Based on the results of the experiments, a strategy for creating a form-fit bond between AlSi10Mg and ABS was suggested in a second stage. This was achieved by combining the FFF process with the PBF-LB process to improve the interfacial strength between AlSi10Mg and ABS.

In order to further investigate the hybrid additive manufacturing, a custom made hybrid machine containing an FFF unit as well as a PBF-LB system is currently under construction. Figure 13 depicts a schematic drawing of the hybrid machine. The use of the hybrid AM system allows the layerwise alternation between the FFF and PBF-LB buildup in the same system, which opens further possibilities in the design of the interface between the FFF and PBF-LB parts. In addition, an optimization of the FFF parameters during overprinting of the initial AlSi10Mg structures is necessary in order to achieve a better bond during continuation of the PBF-LB buildup. Furthermore, an optimization of the PBF-LB processing parameters is necessary. It needs to be analyzed after which layer the laser energy density in the PBF-LB process can be increased to reduce the lack of fusion porosity in the AlSi10Mg without causing thermal degradation of the underlying ABS. Additionally, mechanical tensile tests are planned to quantify the strength of the optimized hybrid components.

Declaration of Competing Interest

The authors declare that they have no known competing financial interests or personal relationships that could have appeared to influence the work reported in this paper.

CRediT authorship contribution statement

Steffen Czink: Conceptualization, Data curation, Writing – review & editing, Methodology, Formal analysis, Writing – original draft. **Victor Lubkowitz:** Conceptualization, Methodology, Writing – review & editing. **Stefan Dietrich:** Conceptualization, Methodology, Writing – review & editing. **Volker Schulze:** Supervision, Writing – original draft, Project administration.

Data availability

Data will be made available on request.

Acknowledgments

References

[1] J.J. Lewandowski, M. Seifi, Metal additive manufacturing: a review of mechanical properties, Annu. Rev. Mater. Res. 46 (1) (2016) 151–186, doi:10.1146/annurev–matsci-070115-032024.

[2] D.D. Gu, W. Meiners, K. Wissenbach, R. Poprawe, Laser additive manufacturing of metallic components: materials, processes and mechanisms, Int. Mater. Rev. 57 (3) (2012) 133–164, doi:10.1179/1743280411Y.0000000014.

[3] M. Schneck, M. Horn, M. Schmitt, C. Seidel, G. Schlick, G. Reinhart, Review on additive hybrid- and multi-material-manufacturing of metals by powder bed fusion: state of technology and development potential, Prog. Addit. Manuf. 6 (4) (2021) 881–894, doi:10.1007/s40964-021-00205-2.

[4] S. Girnth, J. Koopmann, G. Klawitter, N. Waldt, T. Niendorf, 3D hybrid-material processing in selective laser melting: implementation of a selective coating system, Prog. Addit. Manuf. 4 (4) (2019) 399–409, doi:10.1007/s40964-019-00082-w.

[5] J. Koopmann, J. Voigt, T. Niendorf, Additive manufacturing of a steel–ceramic multi-material by selective laser melting, Metall. Mater. Trans. B 50 (2) (2019) 1042–1051, doi:10.1007/s11663-019-01523-1.

[6] T. Feldhausen, B. Yelamanchi, A. Gomez, A. Du plessis, K. Saleeby, K. Fillingim, B. Post, L. Love, P. Cortes, E. MacDonald, Embedding ceramic components in metal structures with hybrid directed energy deposition, Int. J. Adv. Manuf.Technol. (2022), doi:10.21203/rs.3.rs-1749378/v1.

[7] R. Singh, R. Kumar, I. Farina, F. Colangelo, L. Feo, F. Fraternali, Multi-material additive manufacturing of sustainable innovative materials and structures, Polymers 11 (1) (2019), doi:10.3390/polym11010062.

[8] A. Muguruza, J.B. Bo, A. Gómez, J. Minguella-Canela, J. Fernandes, F. Ramos, E. Xuriguera, A. Varea, A. Cirera, Development of a multi-material additive manufacturing process for electronic devices, Procedia Manuf. 13 (2017) 746–753, doi:10.1016/j.promfg.2017.09.180.

[9] E. MacDonald, R. Wicker, Multiprocess 3D printing for increasing component functionality, Science (New York, N.Y.) 353 (6307) (2016), doi:10.1126/science.aaf2093.

[10] M. Baranowski, M. Netzer, P. Gönnheimer, S. Coutandin, J. Fleischer, T. Schlotthauer, P. Middendorf, Functional integration of subcomponents for hybridization of fused filament fabrication, Int. J. Mech. Eng.Rob. Res. (2022) 319–325, doi:10.18178/ijmerr.11.5.319-325.

[11] R. Kurfess, K. Saleeby, T. Feldhausen, B. fillingim, A.J. Hardt, D. Hardt, Towards directed energy deposition of metals using polymer-based supports: porosity of 316l stainless steel deposited on carbon-fiber-reinforced ABS, in: Solid Freeform Fabrication 2022: Proceedings of the 33rd Annual International Solid Freeform Fabrication Symposium – An Additive Manufacturing Conference, 2022. Austin, TX, USA

[12] Y.-H. Chueh, C. Wei, X. Zhang, L. Li, Integrated laser-based powder bed fusion and fused filament fabrication for three-dimensional printing of hybrid metal/polymer objects, Addit. Manuf. 31 (1) (2020) 100928, doi:10.1016/j.addma.2019.100928.

[13] L. Englert, A. Heuer, M.K. Engelskirchen, F. Frölich, S. Dietrich, W.V. Liebig, L. Kärger, V. Schulze, Hybrid material additive manufacturing: interlocking interfaces for fused filament fabrication on laser powder bed fusion substrates, Virtual Phys. Prototyping 17 (3) (2022) 508–527, doi:10.1080/17452759.2022.2048228.

[14] F. Alghamdi, M. Haghshenas, Microstructural and small-scale characterization of additive manufactured AlSi10Mg alloy, SN Appl. Sci. 1 (3) (2019) 22, doi:10.1007/s42452-019-0270-5.

[15] K. Sakunphokesup, P. Kongkrengkrai, A. Pongwisuthiruchte, C. Aumnate, P. Potiyaraj, Graphene-enhanced ABS for FDM 3d printing: effects of masterbatch preparation techniques, IOP Conf. Ser. Mater. Sci.Eng. 600 (1) (2019) 012001, doi:10.1088/1757-899X/600/1/012001.

[16] Z. Li, B.-Q. Li, P. Bai, B. Liu, Y. Wang, Research on the thermal behaviour of a selectively laser melted aluminium alloy: simulation and experiment, Materials (Basel, Switzerland) 11 (7) (2018), doi:10.3390/ma11071172.

[17] J. Wu, L. Wang, X. An, Numerical analysis of residual stress evolution of AlSi10Mg manufactured by selective laser melting, Optik 137 (7) (2017) 65–78, doi:10.1016/j.ijleo.2017.02.060.

[18] BASF 3D Printing Solutions BV, Ultrafuse ABS: Technical Data Sheet, 03.11.2022. https://www.ultrafusefff.com/wp-content/uploads/2016/05/Ultrafuse_ABS_TDS_EN_v5.2.pdf.

[19] M. Suzuki, C.A. Wilkie, The thermal degradation of acrylonitrile-butadiene-styrene terpolymei as studied by TGA/FTIR, Polymer Degradation and Stability 47 (2) (1995) 217–221, doi:10.1016/0141-3910(94)00122-O.

[20] S. Czink, S. Dietrich, V. Schulze, Ultrasonic evaluation of elastic properties in laser powder bed fusion manufactured AlSi10Mg components, NDT & E Int. 132 (1) (2022) 102729, doi:10.1016/j.ndteint.2022.102729.

[21] T. Liu, C.S. Lough, H. Sehhat, Y.M. Ren, P.D. Christofides, E.C. Kinzel, M.C. Leu, In-situ infrared thermographic inspection for local powder layer thickness measurement in laser powder bed fusion, Addit. Manuf. 55 (3) (2022) 102873, doi:10.1016/j.addma.2022.102873.

[22] G. Leuteritz, S. Schudak, M. Rohling, R. Lachmayer, Formschlüssige multimaterielle additive fertigung zur realisierung funktionsintegrierter hybrid-bauteile, in: R. Lachmayer, R.B. Lippert, S. Kaierle (Eds.), Konstruktion für die Additive Fertigung 2018, Vol. 47, Springer Berlin Heidelberg, Berlin, Heidelberg, 2020, pp. 299–317, doi:10.1007/978-3-662-59058-4_17.